







Experimental observation of high intrinsic thermal conductivity of AlN

Zhe Cheng ¹, Yee Rui Koh,² Abdullah Mamun ³, Jingjing Shi,¹ Tingyu Bai,⁴ Kenny Huynh,⁴ Luke Yates,¹ Zeyu Liu,⁵ Ruiyang Li,⁵ Eungkyu Lee,⁵ Michael E. Liao ⁴, Yekan Wang,⁴ Hsuan Ming Yu ⁴, Maki Kushimoto ⁶, Tengfei Luo,⁵ Mark S. Goorsky,⁴ Patrick E. Hopkins,^{2,8,9} Hiroshi Amano,⁷ Asif Khan,³ and Samuel Graham ^{1,10,*}

¹George W. Woodruff School of Mechanical Engineering, Georgia Institute of Technology, Atlanta, Georgia 30332, USA

²Department of Mechanical and Aerospace Engineering, University of Virginia, Charlottesville, Virginia 22904, USA

³Department of Electrical Engineering, University of South Carolina, Columbia, South Carolina 29208, USA

⁴Materials Science and Engineering, University of California, Los Angeles, Los Angeles, California 90095, USA

⁵Department of Aerospace and Mechanical Engineering, University of Notre Dame, Notre Dame, Indiana 46556, USA

⁶Department of Electrical Engineering and Computer Science, Nagoya University, Furo-cho, Chikusa-ku 464-8603, Nagoya, Japan

⁷Institute of Materials and Systems for Sustainability, Nagoya University, Furo-cho, Chikusa-ku 464-8601, Nagoya, Japan

⁸Department of Materials Science and Engineering, University of Virginia, Charlottesville, Virginia 22904, USA

⁹Department of Physics, University of Virginia, Charlottesville, Virginia 22904, USA

¹⁰School of Materials Science and Engineering, Georgia Institute of Technology, Atlanta, Georgia 30332, USA



(Received 15 January 2020; accepted 13 March 2020; published 23 April 2020)

Wurtzite AlN is an ultrawide bandgap semiconductor that has been developed for applications including power electronics and optoelectronics. Thermal management of these applications is the key for stable device performance and allowing for long lifetimes. However, the intrinsic high thermal conductivity of bulk AlN predicted by theoretical calculations has not been experimentally observed because of the difficulty in producing high-quality materials. This work reports the growth of thick ($>15 \mu\text{m}$) AlN layers by metal-organic chemical vapor deposition and experimental observation of intrinsic thermal conductivity from 130 to 480 K that matches density-functional-theory calculations for single crystal AlN, producing some of the highest values ever measured. Detailed material characterizations confirm the high quality of these AlN samples with one or two orders of magnitude lower impurity concentrations than commercially available bulk AlN. The thermal conductivity of these commercially available bulk AlN substrates are also measured as comparison. To interpret the reduced thermal conductivity, a simple Callaway model is built. This work demonstrates the possibility of obtaining theoretically high values of thermal conductivity in AlN and will impact the thermal management and reliability of future electronic and optoelectronics devices.

DOI: [10.1103/PhysRevMaterials.4.044602](https://doi.org/10.1103/PhysRevMaterials.4.044602)

I. INTRODUCTION

Aluminum nitride (AlN) is an ultrawide bandgap semiconductor which has been developed for applications of power electronics and optoelectronics such as next-generation ultraviolet (UV) light-emitting diodes (LED) and laser diodes [1]. The thermal management of these devices is the key for stable performance and long lifetime, especially for high-power and high-frequency power electronics and high-power optoelectronics. For instance, the external quantum efficiency of deep UV-carbon (C) (100–280 nm) LEDs is typically in the single-digit percent range, even less than 1% for LEDs with wavelength shorter than 250 nm [2,3]. The majority of the input power is converted to Joule heating, which raises the LED temperature and forms a hotspot in the junction area. The device temperature is a critical factor which significantly affects the wavelength, reliability, and lifetime and correspondingly limits the maximum output power of UV LEDs [2]. Moreover, wide bandgap materials as substrates are critical for UV-C LEDs in order to provide the necessary

optical transparency for light extraction. In other applications beyond optoelectronics, wide bandgap materials such as AlN are used as interfacial layers or growth substrates in devices requiring the heteroepitaxial growth of wide bandgap power or radio frequency semiconductors like GaN and Ga₂O₃, both also require similar attention to manage their temperature rise. Therefore, materials with wide bandgaps and high thermal conductivity such as AlN are of importance in several technologically important applications that require efficient heat dissipation to ensure proper device operation.

Even though it was synthesized more than one century ago, the thermal conductivity of AlN was reported to be about $1.76 \text{ W m}^{-1} \text{ K}^{-1}$ at room temperature in 1959, and about $30 \text{ W m}^{-1} \text{ K}^{-1}$ at 473 K in the form of hot-pressed powder in 1960 due to the delayed development of thermal characterization techniques [4,5]. Until 1973, the thermal conductivity of single crystal AlN was reported to be $200 \text{ W m}^{-1} \text{ K}^{-1}$ at room temperature with high concentrations of oxygen impurities and later increased to $285 \text{ W m}^{-1} \text{ K}^{-1}$ with improved quality in 1987 [6–8]. After that, more thermal studies were performed on AlN ceramics and commercial AlN substrates but no higher thermal conductivity values were observed [9–13]. This value ($285 \text{ W m}^{-1} \text{ K}^{-1}$) has been

*Corresponding author: sgraham@gatech.edu

widely accepted as the room-temperature thermal conductivity of bulk AlN for decades, even though the calculated intrinsic thermal conductivity was reported by Slack in 1973 to be $320 \text{ W m}^{-1} \text{ K}^{-1}$, close to first-principles-calculated values (318 W/m K) [6,13]. This higher value was obtained by extrapolating the value of thermal conductivity to the case where the oxygen impurity concentrations is zero. However, no experimental observation of this high value of thermal conductivity has been reported because of the difficulty in growing AlN materials with such low vacancy and impurity levels, and addressing other associated defect complexes in AlN [14–18].

This work demonstrates a high-quality and high-purity AlN film that meets the previous theoretical predictions of high thermal conductivity. The thick single-crystal AlN films were grown by metal-organic chemical vapor deposition (MOCVD) on (0001) sapphire substrates with an air-pocketed AlN layer at the sapphire interface. This layer allows for the growth of thick AlN without any cracking. The thermal conductivity was determined using time-domain thermoreflectance (TDTR), while density functional theory (DFT) was used to calculate the thermal conductivity of perfect single crystal AlN to compare with the measured results. Additionally, the thermal conductivity of two commercially available single-crystal AlN substrates were also measured to compare with the MOCVD samples. Detailed material characterization including scanning transmission electron microscopy (STEM), triple-axis x-ray diffraction, and secondary-ion mass spectrometry (SIMS) were used to verify the crystal quality and purity and help to interpret the measured thermal conductivity data. Finally, a Callaway model was also built to understand the origin of the reduced thermal conductivity of the two commercially available single-crystal AlN substrates.

II. METHODS

A. Sample growth

The AlN growth for this study was carried out using a custom MOCVD reactor. The growth reactor had a fast metal-organic precursor switching manifold. Two-inch diameter 0.2° off-axis basal plane sapphire substrates were used for all the growths. The growth procedure started with a pulsed high-temperature (1373 K) epitaxy sequence where the Al and N precursors (Trimethyl aluminum and NH_3) were alternately supplied to the growth chamber. The Al-N precursor flow rate and the V/III ratio are adjusted to yield air-pocketed AlN layers at the sapphire interface. The air pockets help managing the strain and thus allow the growth of AlN layers with thicknesses well over $15 \mu\text{m}$ without any cracking. Subsequently the growth temperature is increased to 1473 K and the flows are modified to yield smooth layers. From the transition of the low-quality air-pocketed AlN layer to the high-quality AlN grown on its top during the MOCVD growth process, a significant reduction in the number of defects is observed due to dislocation bending/annihilation and cracking is avoided due to strain relief from the air pockets at the interface. A chamber pressure of 40 torr was maintained during the entire two-step growth process. The high growth temperatures and the purity of the growth-precursors leads to a significant reduction in the

incorporation of oxygen, carbon, and other impurities in our MOCVD grown layers. The layer thicknesses were measured from a cross-section image obtained using a scanning electron microscope. The surface quality was then characterized using an atomic force microscope and the RMS value of surface roughness was measured to be 0.25 nm . The off-axis (102) x-ray linewidth was measured to be around 350 arcsec . Based on our previous correlation studies, using etch pit density as a measure of the defects, we estimated the dislocation density in our studied layers to be around $(1 - 3 \times 10^8 \text{ cm}^{-2})$.

B. Thermal characterizations

TDTR is a pump-probe technique that can be used to measure thermal properties of both nanostructured and bulk materials [19,20]. The AlN surface was first coated with a layer of Al ($\sim 80 \text{ nm}$) as the transducer. The local Al thickness is determined by the picosecond acoustic technique [21]. A modulated pump beam (400 nm) heats the sample surface, while a delayed probe beam (800 nm) detects the temperature variation of the sample surface via thermoreflectance. The delay time is controlled by a mechanical delay stage and the signal is picked up by a photodetector and a lock-in amplifier. The pump and probe beam sizes are 19.0 and $13.3 \mu\text{m}$ (diameters) and the modulation frequency is 3.6 MHz . The measured signal is fitted with an analytical heat conduction solution of the multilayer sample structure to infer unknown parameters [20,22]. For samples in this work, the unknown parameters are the Al-AlN thermal boundary conductance and the AlN thermal conductivity. There are three layers for Samp_1 and Samp_2. But the AlN are thermally thick for most of the temperature points and the fitting results of the three-layer model (Al + AlN + sapphire) are very close to the two layer model (Al + AlN). The Al heat capacity, AlN heat capacity, sapphire heat capacity, Al thermal conductivity, and sapphire thermal conductivity are from the literature [23–25]. The TDTR sensitivity and data fitting can be found in the Supplemental Material [26]. In this work, TDTR is only sensitive to the cross-plane thermal conductivity and we do not consider anisotropic thermal conductivity in the data fitting because the sensitivity of in-plane thermal conductivity is small and anisotropy of AlN thermal conductivity is not strong. We used a Monte Carlo method to calculate the errors of these TDTR measurements and more details are included in the Supplemental Material [26].

C. DFT calculation

An iterative scheme is applied to solve the linearized phonon Boltzmann transport equation with the help of first-principles force constants. We first relax the AlN atomic structure to its optimized positions using QUANTUM ESPRESSO [28]. Then second order force constants, which provide phonon frequencies, group velocity, and scattering phase space, are calculated using density functional perturbation theory, using an $8 \times 8 \times 4 q$ space grid. Finite difference methods implemented in `thirdorder.py` [29] are used to calculate third order force constants in order to calculate three-phonon scattering rates based on a $4 \times 4 \times 4$ supercell. The linearized phonon

Boltzmann transport equation (BTE) is solved iteratively using SHENGBTE in a $12 \times 12 \times 12$ Monkhorst-Pack grid [29]

D. Callaway model

The thermal conductivity of nonmetal crystalline material can be expressed as [30–33]

$$k = \frac{1}{3} \sum_p \int_0^{\omega_{\text{cut-off}}} \hbar \omega D_\lambda \frac{d f_{BE}}{dT} v_\lambda^2 \tau_{C,\lambda}, \quad (1)$$

where ω is the phonon frequency, \hbar is the reduced Planck constant, v_λ is the modal phonon group velocity of phonon mode λ , $\tau_{C,\lambda}$ is the modal combined relaxation time, \sum_p is over all phonon polarizations, and D_λ is the modal phonon density of states, and f_{BE} is the Bose-Einstein distribution function. The combined relaxation time $\tau_{C,\lambda}$ of each phonon mode can be obtained from the Matthiessen's rule as [32,33]

$$\tau_{C,\lambda} = \left(\frac{1}{\tau_U} + \frac{1}{\tau_M} + \frac{1}{\tau_B} \right)^{-1}, \quad (2)$$

where τ_U , τ_M , and τ_B are the relaxation times of Umklapp phonon-phonon scattering, mass-difference phonon-impurity scattering, and phonon-boundary scattering, respectively. The scattering rate expressions are [13,34–36]

$$\frac{1}{\tau_U} = B T \omega^2 e^{-\frac{c}{T}}, \quad (3)$$

$$\frac{1}{\tau_M} = \frac{V \omega^4}{4\pi v^3} \sum_i x_i \left(\frac{\Delta M_i}{M} \right)^2, \quad (4)$$

$$\frac{1}{\tau_B} = v/d, \quad (5)$$

where B and C are fitting parameters, V is the volume of the AlN primitive cell, x_i is the atomic fraction of sites occupied by defect i , ΔM_i is the mass difference between defect and original atom, and d is the thickness of the AlN sample. To calculate the scattering rates of different mechanisms, the parameters B and C are fitted with the first-principle-calculated AlN thermal conductivity. The impurity scattering rates of C, O, and Si are calculated based on the SIMS results. Additionally, the Al vacancies are also considered and the vacancy concentrations are obtained by fitting the analytical predictions with experimental measurements.

E. Raman spectroscopy

We employed Raman spectroscopy to analyze the 18- μm AlN film, with a Renishaw InVia system using a 50x objective lens and 488-nm laser. All symmetry-allowed optical phonons in AlN film are dominated by the E_2 mode, followed by weaker $A_1(\text{LO})$, $A_1(\text{TO})$, and $E_1(\text{TO})$ modes, where TO is transverse optical mode, and LO is longitudinal optical mode. Weak Raman spectra for the substrate, Al_2O_3 , can also be observed in the analysis.

III. RESULTS AND DISCUSSION

For this study, four separate AlN samples were chosen for thermal conductivity measurements. Samp_1 and Samp_2 were grown by MOCVD on sapphire substrates with AlN

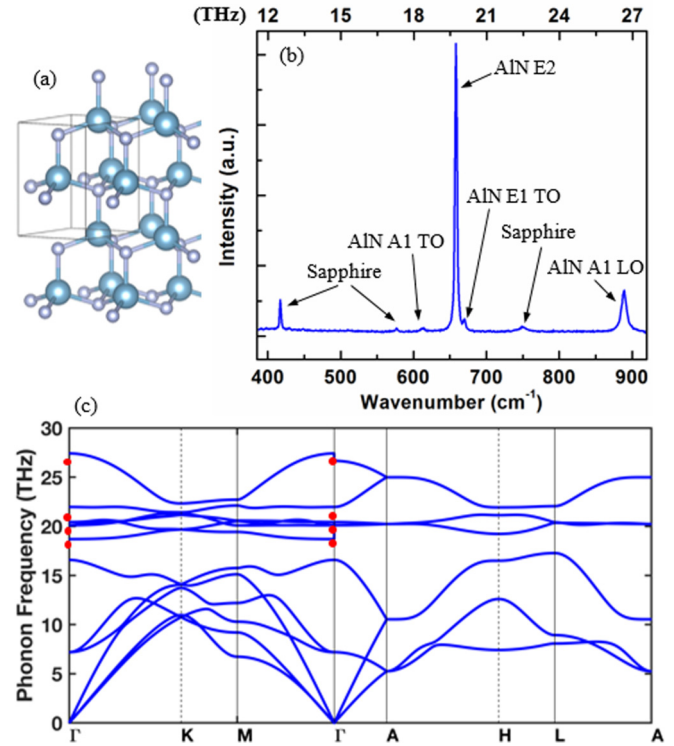


FIG. 1. (a) Crystal structure of AlN. (b) Raman spectroscopy of Samp_2. (c) Phonon dispersion relation of AlN calculated by DFT. The red dots are Raman peak frequencies at the gamma point.

thicknesses of 18 and 22.5 μm , respectively. Samp_3 and Samp_4 (~ 500 - μm -thick wafers) are purchased from HexaTech, Inc. and grown by physical vapor transport (PVT) [37]. As shown in Fig. 1(a), the AlN studied in this work has a wurtzite crystal structure and four atoms in one unit cell. Figure 1(b) shows the Raman spectrum of Samp_2. The Raman peaks are A1 (TO) with phonon frequency of 18.37 THz, E_2 with phonon frequency of 19.74 THz, E_1 (TO) with phonon frequency of 20.09 THz, and A1 (LO) with phonon frequency of 26.65 THz [38]. The other three peaks are from the sapphire substrates [39]. All the Raman peaks are clean and sharp. This observation verified that the AlN film is high quality, and no intermixing of the impurities and substances was present in the film.

We also calculated the Raman peaks and compared with the measured Raman data, as shown in Table I. All Raman peaks and linewidths are generated from fitting a mixture of Lorentzian functions. The DFT results agree well in the phonon mode frequency. For the linewidth, the DFT results are very close to the Raman data except A1(LO) mode, where the DFT calculated linewidth is much smaller than the measurement result. This disagreement may come from the quality of the sample and the substrate. It should also be noted that the linewidths of E_2 and $E_1(\text{TO})$ modes in DFT simulation are smaller than the measurement data. One possible reason is that the simulation utilizes a Gaussian function with finite width to replace Dirac δ function for the conservation of energy and considering the fact that these two modes are close in their frequencies. This Gaussian smearing will lead to an effect of mixing of these two modes and result

TABLE I. Comparison of measured Raman data and DFT-predicted Raman data.

	A1(TO)	E2	E1(TO)	A1(LO)
Raman peak (THz)	18.37	19.74	20.09	26.65
DFT peak (THz)	18.70	20.11	20.43	27.42
Raman width (THz)	0.1269	0.0445	0.03296	0.1200
DFT width (THz)	+/- 0.0399	+/- 0.0002	+/- 0.00686	+/- 0.0014
	0.0884	0.0573	0.0581	0.0246

in similar lifetimes. This can effectively increase the simulated linewidth for these two modes.

Figure 1(c) shows the phonon dispersion relation of AlN calculated by DFT. AlN has three acoustic phonon branches and nine optical branches. The phonon frequencies of polarized materials approaching the gamma point from different directions are different, which results in the frequency discontinuous points at the gamma point. In terms of AlX compounds ($X = N, P, As,$ and Sb), AlN has the largest acoustic phonon frequency scale and the highest acoustic velocities, resulting in high thermal conductivity [40]. There is no appreciable phonon band gap between acoustic and optical phonon branches of AlN that enables extensive acoustic phonon-optical phonon scattering, which decreases the thermal conductivity of AlN rapidly with increasing temperature at relatively high temperatures [40].

Figure 2(a) shows the high-resolution TEM image along the [1100] zone axis of Samp_1, which shows distinct lattice planes without any visible lattice defects. To study the structure of the MOCVD grown AlN, Fig. 2(b) shows the near-surface cross-sectional STEM image of AlN of Samp_1. A few dislocations show up along the growth direction.

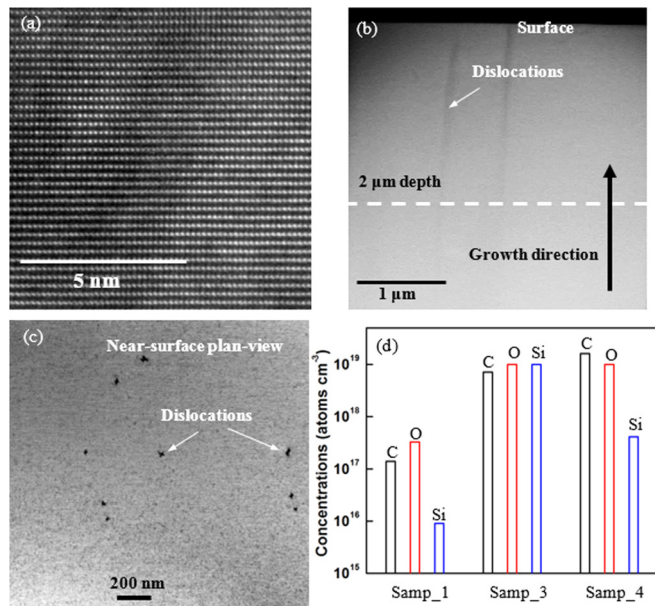


FIG. 2. (a) High resolution TEM image along [1100] zone axis of Samp_1. (b) Near-surface cross-section image of AlN grown on sapphire substrates of Samp_1. (c) Near-surface plan-view STEM image of Samp_1. (d) Impurity concentrations of carbon (C), oxygen (O), and silicon (Si) of Samp_1, Samp_3, and Samp_4 measured by SIMS.

Figure 2(c) shows the near-surface plan-view STEM image of Samp_1 with some dislocations. The dislocation density of Samp_1 and Samp_2, which were grown on sapphire, is estimated to be $1.6 \times 10^8 \text{ cm}^{-2}$, while that of Samp_3 and Samp_4 (commercially available bulk materials) are several orders of magnitude lower ($2.2 \times 10^4 \text{ cm}^{-2}$). More details about the TEM and x-ray topography studies to determine dislocation density can be found in the Supplemental Material (Figs. S1 and S2) [26]. Although the dislocation density is higher in the heteroepitaxially MOCVD grown material than the bulk PVT samples, we expect this dislocation density to have a negligible impact on the thermal conductivity [41]. Moreover, the dislocations are aligned along the c -axis direction, which affects cross-plane thermal conductivity less than the in-plane thermal conductivity. Based on our laser spot size, our TDTR measurements are more sensitive to the cross-plane thermal conductivity. To compare the impurity concentrations in these samples, SIMS is used to measure the concentrations of carbon (C), oxygen (O), and silicon (Si) of Samp_1, Samp_3, and Samp_4. As shown in Fig. 2(d), the impurity concentrations of Samp_1 is one or two orders of magnitude lower than that of Samp_3 and Samp_4, indicating the higher purity of the MOCVD samples.

The temperature dependent thermal conductivities of Samp_1 and Samp_2 are shown in Fig. 3(a) and are compared with DFT calculations. Round-robin measurements were performed at room temperature by TDTR in three different laboratories (Georgia Tech, University of Virginia, and University of Notre Dame) and consistent results were obtained. The error bars are calculated with a Monte Carlo method by considering all possible errors [26]. The DFT calculations for the thermal conductivity at low temperatures (“DFT_Lindsay”) is from the literature [40] and the DFT calculated thermal conductivity at high temperatures is from this work. Excellent agreement between experimentally measured thermal conductivity and DFT-calculated thermal conductivity is achieved from 130 to 480 K, which highlights the high quality of the MOCVD-grown AlN and confirms that the dislocations and small amounts of impurities have a negligible impact on measured thermal conductivity in Samp_1 and Samp_2. Here, TDTR measurements only probe the top portion of the thick films and any defects near the growth interface are not sampled by the analysis even at temperatures as low as 130 K.

Figure 3(b) shows the historical reporting of experimentally measured thermal conductivity of AlN [4,6–13]. Please note that the reported value of AlN thermal conductivity ($1.76 \text{ W m}^{-1} \text{ K}^{-1}$) in 1959 is very low so we did not plot it in Fig. 3(b) considering the scale of the graph. The thermal conductivity data reported in 1960 is at 473 K in the form of hot-pressed AlN powder [4]. All the other values are room-temperature values. The red line is the DFT-calculated

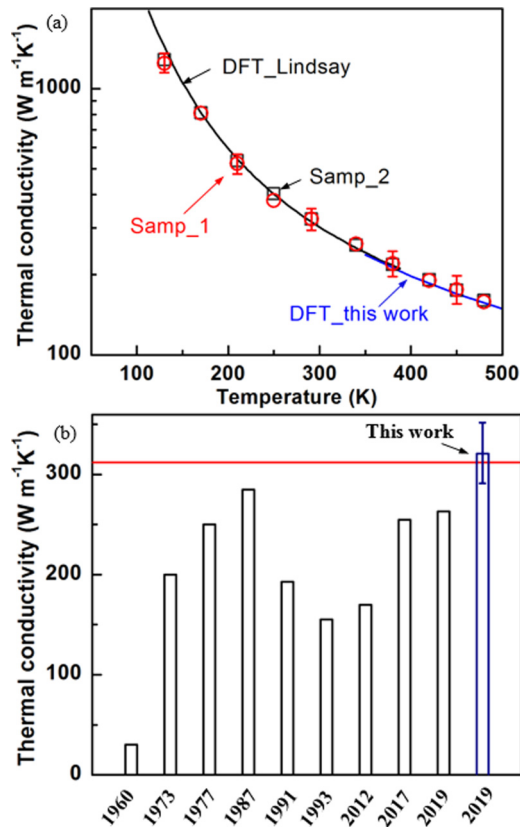


FIG. 3. (a) Temperature dependent thermal conductivity of Samp_1 and Samp_2, and first-principles calculated temperature dependent thermal conductivity of single crystal AlN. (b) The experimentally measured thermal conductivity of AlN reported with time [4,6–13]. The data in 1960 is at 473 K and all the other values are room-temperature values [4]. The red line is DFT-calculated theoretical value of AlN thermal conductivity.

theoretical value of AlN thermal conductivity. As shown in Fig. 3(b), the thermal conductivity reported in this work for Samp_1 and Samp_2 is the highest reported thermal conductivity of AlN, which matches the DFT-calculated theoretical predictions. This is due to the high quality of these MOCVD grown samples that will be discussed in detail later. Our measured thermal conductivity ($321 W m^{-1} K^{-1}$) in this work clearly shows that the widely used value of $285 W m^{-1} K^{-1}$ for bulk AlN can be exceeded.

For comparison with the two MOCVD-grown AlN samples, two commercially available AlN substrates grown by PVT were measured by TDTR (Samp_3 and Samp_4). The measured thermal conductivities of these four samples are summarized in Fig. 4(a). The thermal conductivities of Samp_3 and Samp_4 are lower than the MOCVD samples at all temperature points. The thermal conductivity of Samp_3 and Samp_4 at room temperature are 278 and $216 W m^{-1} K^{-1}$, close to literature values for samples from this source [13]. It has been reported that Al vacancies play a dominant role in limiting the thermal conductivity of these commercially available PVT AlN substrates [13]. There might be other vacancies in our samples. Due to the difficulty to quantify vacancy types and concentrations experimentally, we only consider Al vacancies here. To understand the measured

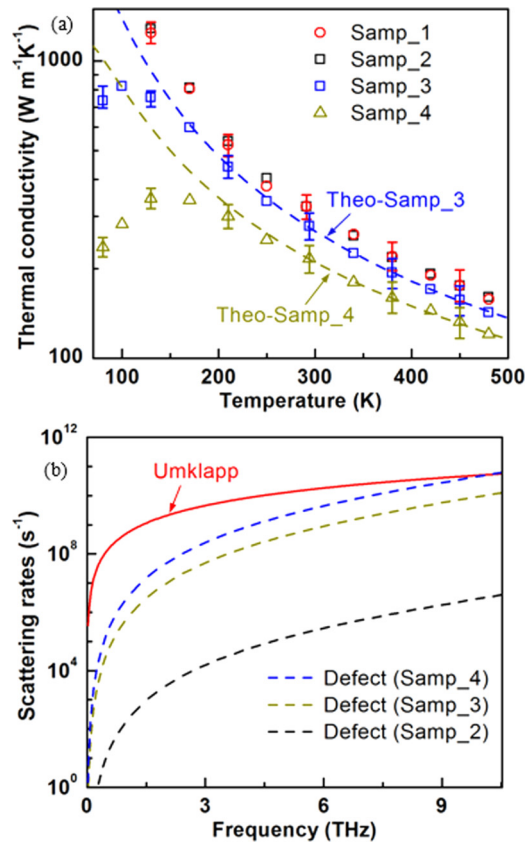


FIG. 4. (a) Measured temperature dependent thermal conductivity of Samp_1, Samp_2, Samp_3, and Samp_4. The dashed lines are theoretical fitting curves by considering the effects of impurities and vacancies. (b) Scattering rates for different scattering sources: phonon-phonon Umklapp scattering, and phonon-defects scatterings, including impurities and vacancies.

thermal conductivities of Samp_3 and Samp_4, we used a Callaway thermal model employing full phonon dispersion relations and Matthiessen’s rule to account for different phonon scattering mechanisms. Defect-phonon scattering rate is proportional to the square of mass difference ratio. The mass of a vacancy is zero so phonon-vacancy scattering has a very large mass difference ratio and a correspondingly large phonon-vacancy scattering rate, leading to significantly reduced thermal conductivity. Our Callaway model includes the effect of impurity-phonon scattering (C, O, Si) and phonon-vacancy scattering. Because it is very challenging to measure the vacancy concentration in AlN, we infer the Al vacancy concentration by fitting the temperature dependent thermal conductivity data. The Al vacancy concentrations in Samp_1 and Samp_2 are negligible. The Al vacancy concentrations for Samp_3 and Samp_4 are estimated to be $3 \times 10^{19} cm^{-3}$ and $1.5 \times 10^{20} cm^{-3}$, which are comparable or higher than the impurity concentrations. Please note that this is a first-order estimation because an accurate calculation method including impurities or even defect complexes are under development. Here, we assume all the impurities and vacancies are point defects and the scattering rates calculation are based on Eqs. (3)–(5). We attribute the large deviations between experimental data and Callaway model data at low temperatures to

the limitation of the Callaway model and possible other scattering mechanisms [42]. It is notable that the variation of interatomic force constants is not included in the Callaway model to calculate scattering rates, which affects defect/vacancy-phonon scatterings and subsequently thermal conductivity [43,44]. Figure 4(b) shows the scattering rates of different samples at room temperature. The defects scattering rates of all samples are lower than the phonon-phonon Umklapp scattering rates at the whole acoustic phonon frequency range. All these scattering rates increase with frequency because low frequency phonons are less scattered by other phonons and structural imperfections. The defects scattering rates of Samp_3 and Samp_4 are much higher than that of Samp_2 due to the different impurity (C, O, and Si) and Al vacancy concentrations. Overall, combining the thermal characterizations and materials structural characterizations, Samp_1 and Samp_2 grown by MOCVD have much lower point defect levels in terms of impurities and vacancies than commercially available PVT-grown Samp_3 and Samp_4. Additionally, the AlN/sapphire substrates are a very cost-effective solution with one order of magnitude reduction in cost. More cost information can be found in the Supplemental Material [26].

IV. CONCLUSIONS

In this work, we reported an experimental observation of the intrinsic thermal conductivity of AlN grown by MOCVD from 130 to 480 K, which matches excellently with DFT-predicted thermal conductivity of single crystal AlN. SIMS measurements show that the MOCVD AlN samples have one or two orders of magnitude lower impurity concentrations

(C, O, and Si) than the commercially available PVT substrates, despite our MOCVD AlN having a dislocation density several orders of magnitude higher than the commercial substrates. For comparison, two commercially available PVT AlN substrates were measured from 80 to 480 K and the measured thermal conductivity were close to literature values of samples from the same supplier. Moreover, the results of this work demonstrate that it is possible to grow thick films of high thermal conductivity AlN for heat dissipation applications in wide bandgap electronics with thermal conductivity values that exceed the bulk material available today. The lower thermal conductivity values in commercially available bulk substrates are attributed to possible high concentrations of Al vacancies and/or vacancy-impurity complexes. Our work clearly shows that MOCVD can be employed to grow thick AlN films with thermal properties that match theoretical predictions. This result may open new doors for research with AlN both from fundamental thermal science to semiconductor growth, especially in applications where thermal management is of high importance.

ACKNOWLEDGMENTS

The authors would like to acknowledge the financial support from Office of Naval Research MURI Grant No. N00014-18-1-2429. The x-ray topography study used resources of the Advanced Photon Source, a US Department of Energy (DOE) Office of Science User Facility operated for the DOE Office of Science by Argonne National Laboratory under Contract No. DE-AC02-06CH11357.

The authors claim no competing financial interest.

-
- [1] J. Tsao, S. Chowdhury, M. Hollis, D. Jena, N. Johnson, K. Jones, R. Kaplar, S. Rajan, C. Van de Walle, E. Bellotti, C. Chua, R. Collazo, M. Coltrin, J. Copper, K. Evans, S. Graham, T. Grotjohn, E. Heller, M. Higashiwaki, M. Islam, P. Juodawlkis, M. Khan, A. Koehler, J. Leach, U. Mishra, R. Nemanich, R. Pilawa-Podgurski, J. Shealy, Z. Sitar, M. Tadjer, A. Witulski, M. Wraback, and J. Simmons, *Adv. Electron. Mater.* **4**, 1600501 (2018).
 - [2] M. Kneissl, T.-Y. Seong, J. Han, and H. Amano, *Nat. Photon.* **13**, 233 (2019).
 - [3] A. Khan, K. Balakrishnan, and T. Katona, *Nat. Photon.* **2**, 77 (2008).
 - [4] K. Taylor and C. Lenie, *J. Electrochem. Soc.* **107**, 308 (1960).
 - [5] G. Long and L. Foster, *J. Am. Ceram. Soc.* **42**, 53 (1959).
 - [6] G. A. Slack, *J. Phys. Chem. Solids* **34**, 321 (1973).
 - [7] G. Slack and T. McNelly, *J. Cryst. Growth* **42**, 560 (1977).
 - [8] G. A. Slack, R. A. Tanzilli, R. Pohl, and J. Vandersande, *J. Phys. Chem. Solids* **48**, 641 (1987).
 - [9] R. R. Lee, *J. Am. Ceram. Soc.* **74**, 2242 (1991).
 - [10] A. Geith, M. Kulig, T. Hofmann, and C. Rüssel, *J. Mater. Sci.* **28**, 865 (1993).
 - [11] C. Duquenne, M.-P. Besland, P. Tessier, E. Gautron, Y. Scudeller, and D. Averty, *J. Phys. D* **45**, 015301 (2011).
 - [12] Y. Shen, J. Gaskins, X. Xie, B. M. Foley, R. Cheaito, P. E. Hopkins, and J. C. Campbell, *J. Lightwave Tech.* **35**, 4242 (2017).
 - [13] R. L. Xu, M. Muñoz Rojo, S. M. Islam, A. Sood, B. Vareskic, A. Katre, N. Mingo, K. E. Goodson, H. G. Xing, D. Jena, and E. Pop, *J. Appl. Phys.* **126**, 185105 (2019).
 - [14] N. Nepal, M. Nakarmi, J. Lin, and H. Jiang, *Appl. Phys. Lett.* **89**, 092107 (2006).
 - [15] K. Nam, M. Nakarmi, J. Lin, and H. Jiang, *Appl. Phys. Lett.* **86**, 222108 (2005).
 - [16] T. Schulz, M. Albrecht, K. Irmscher, C. Hartmann, J. Wollweber, and R. Fornari, *Phys. Status Solidi B* **248**, 1513 (2011).
 - [17] R. Collazo, J. Xie, B. Gaddy, Z. Bryan, R. Kirste, M. Hoffmann, R. Dalmau, B. Moody, Y. Kumagai, T. Nagashima, Y. Kubota, T. Kinoshita, A. Koukitu, D. Irving, and Z. Sitar, *Appl. Phys. Lett.* **100**, 191914 (2012).
 - [18] B. E. Gaddy, Z. Bryan, I. Bryan, J. Xie, R. Dalmau, B. Moody, Y. Kumagai, T. Nagashima, Y. Kubota, T. Kinoshita, A. Koukitu, R. Kirste, Z. Sitar, R. Collazo, and D. Irving, *Appl. Phys. Lett.* **104**, 202106 (2014).
 - [19] D. G. Cahill, *Rev. Sci. Instrum.* **75**, 5119 (2004).
 - [20] Z. Cheng, T. Bougher, T. Bai, S. Y. Wang, C. Li, L. Yates, B. M. Foley, M. Goorsky, B. A. Cola, F. Faili, and S. Graham, *ACS Appl. Mater. Interf.* **10**, 4808 (2018).
 - [21] Z. Cheng, L. Yates, J. Shi, M. J. Tadjer, K. D. Hobart, and S. Graham, *APL Mater.* **7**, 031118 (2019).
 - [22] Z. Cheng, T. Bai, J. Shi, T. Feng, Y. Wang, M. Mecklenburg, C. Li, K. D. Hobart, T. Feygelson, M. Tadjer, B. Pate, B. Foley,

- L. Yates, S. Pantelides, B. Cola, M. Goorsky, and S. Graham, *ACS Appl. Mater. Interfaces* **11**, 18517 (2019).
- [23] Z. Cheng, Y. Koh, H. Ahmad, R. Hu, J. Shi, M. Liao, Y. Wang, T. Bai, R. Li, E. Lee, E. Clinton, C. Matthews, Z. Engel, L. Yates, T. Luo, M. Goorsky, W. Doolittle, Z. Tian, P. Hopkins, and S. Graham, [arXiv:1906.05484](https://arxiv.org/abs/1906.05484) (2019).
- [24] D. Sedmidubský, J. Leitner, P. Svoboda, Z. Sofer, and J. Macháček, *Nature* **461**, 403 (2009).
- [25] F. Mu, Z. Cheng, J. Shi, S. Shin, B. Xu, J. Shiomi, S. Graham, and T. Suga, *ACS Appl. Mater. Interf.* **11**, 33428 (2019).
- [26] See Supplemental Material at <http://link.aps.org/supplemental/10.1103/PhysRevMaterials.4.044602> for the cost information about the AlN growth, the characterization of dislocation density by TEM and x-ray topography study, the details of data fitting and error calculation of TDTR measurements, and the details about DFT calculations. See also Ref. [27].
- [27] T. L. Bougher, L. Yates, C.-F. Lo, W. Johnson, S. Graham, and B. A. Cola, *Nano. and Micro. Thermophys. Engineer.* **20**, 22 (2016).
- [28] P. Giannozzi, S. Baroni, N. Bonini, M. Calandra, R. Car, C. Cavazzoni, D. Ceresoli, G. Chiarotti, M. Cococcioni, I. Dabo, A. Corso, S. Gironcoli, S. Fabris, G. Fratesi, R. Gebauer, U. Gerstmann, C. Gougousis, A. Kokalj, M. Lazzeri, L. Martin-Samos, N. Marzari, F. Mauri, R. Mazzarello, S. Paolini, A. Pasquarello, L. Paulatto, C. Sbraccia, S. Scandolo, G. Sclauzero, A. Seitsonen, A. Smogunov, P. Umari, and R. Wentzcovitch, *J. Phys.: Condens. Matter* **21**, 395502 (2009).
- [29] W. Li, J. Carrete, N. A. Katcho, and N. Mingo, *Comput. Phys. Commun.* **185**, 1747 (2014).
- [30] J. Callaway, *Phys. Rev.* **113**, 1046 (1959).
- [31] N. Mingo, *Phys. Rev. B* **68**, 113308 (2003).
- [32] T. Feng and X. Ruan, *Phys. Rev. B* **93**, 045202 (2016).
- [33] Z. Cheng, B. M. Foley, T. Bougher, L. Yates, B. A. Cola, and S. Graham, *J. Appl. Phys.* **123**, 095114 (2018).
- [34] P. Klemens, *Proc. Phys. Soc. Sec. A* **68**, 1113 (1955).
- [35] W. Liu and A. A. Balandin, *J. Appl. Phys.* **97**, 073710 (2005).
- [36] A. Szein, J. Haberstroh, J. E. Bowers, S. P. DenBaars, and S. Nakamura, *J. Appl. Phys.* **113**, 183707 (2013).
- [37] <http://www.hexatechinc.com/aln-growth-process.html>.
- [38] W. Zheng, R. Zheng, F. Huang, H. Wu, and F. Li, *Photon. Res.* **3**, 38 (2015).
- [39] M. Kadleiková, J. Breza, and M. Veselý, *Microelectronics J.* **32**, 955 (2001).
- [40] L. Lindsay, D. A. Broido, and T. L. Reinecke, *Phys. Rev. B* **87**, 165201 (2013).
- [41] B. Sun, G. Haunschild, C. Polanco, L. Lindsay, G. Koblmüller, and Y. K. Koh, *Nat. Mater.* **18**, 136 (2019).
- [42] Y. Sun, Y. Zhou, J. Han, W. Liu, C. Nan, Y. Lin, M. Hu, and B. Xu, *npj Comput. Mater.* **5**, 1 (2019).
- [43] C. A. Polanco and L. Lindsay, *Phys. Rev. B* **98**, 014306 (2018).
- [44] N. A. Katcho, J. Carrete, W. Li, and N. Mingo, *Phys. Rev. B* **90**, 094117 (2014).